A Robust Calibration and Alignment Procedure for Collocated Magnetometer and Accelerometer Sensors

Troy C. Richards and Carmen E. Lucas

Defence Research and Development Canada

June 16, 2015

Abstract

To simplify the task of aligning three-axis magnetometers to a horizontal, vertical, and magnetic north reference frame on the seafloor, as required for ship signature measurements, a three-axis accelerometer can be rigidly mounted to the magnetometer and the measured accelerations used to rotate the data to the required reference frame. We present a calibration procedure that corrects for scale and orthogonality errors of the magnetometer, computes a cross-talk and offset model for the accelerometer, and then determines rotation angles to align the magnetometer and accelerometer axes. The key to the procedure is the design of a solenoid which creates a highly uniform magnetic field over a large volume within the solenoid. The solenoid design begins with a conventional approach using equally spaced concentric loops with the same number of turns, but then allows the current in a number of the outer loops to vary over a continuous range (as required for optimization). Then for a realizable design, the optimum ampere turns are rounded to an integer value, and the magnetic field is re-optimized by varying the position of the same loops. After construction, the solenoid itself was calibrated using a scalar magnetometer. To determine the calibration coefficients the sensors under test are placed within the uniform magnetic field at a number of nominal orientations and a very low frequency current is applied. As the procedure works with the magnitudes of the magnetic and gravitational fields the precise orientations of the sensors within the solenoid are not required.

1. Introduction

The use of three-axis flux-gate magnetometers for measuring the magnetic signature of vessels is common practise in today's Navies. To alleviate the difficult task of accurately orienting the magnetometers to horizontal, vertical and magnetic north, when the sensors are on the seafloor, magnetometers are collocated with three-axis accelerometers, which allows the required orientation of the magnetic data to be automated using the measured gravity accelerations. It is often the case, however, that the magnetometer and accelerometer are calibrated individually and not together as a combined sensor.

Variations and distortions of the earth's magnetic field make the calibration of magnetic field sensors particularly challenging, with urban environments being the worst case, due to magnetic contamination from all sorts of sources including passing cars, trains, and ships, in the vicinity, or nearby objects, like moving chairs and even personnel with magnetic material, all of which can create undesired anomalies and hamper the calibration process. To separate the signals under test from the ever present earth's magnetic field some researchers have tried rotating the sensor in a magnetically quiet area with a low spatial gradient [1]. Such areas however can be difficult to find since the earth's crust contains significant magnetic material itself, which create large gradients, often greater than 100 nT/m. Inside office buildings, and laboratories, with steel beams (where the work described here was done) magnetic gradients can easily exceed 1000 nT/m.

Our specific project, which would ultimately look at electric fields as well, led to the decision to use a fibreglass cylinder of approximately 3 m in length with a diameter of 1.6 m. The basic idea being that the cylinder could be submerged in a salt water tank with conductive plates on either end, to produce electric fields, and also wrapped with wire creating a solenoid to produce magnetic fields.

From these nominal design parameters we investigated the magnetic field uniformity inside a solenoid by superimposing the contribution of very small wire segments, describing the windings of a solenoid, according to the Biot-Savart law. From this initial investigation we determined the approximate number of turns per meter required to achieve reasonable field levels, and that for the best uniformity the solenoid should be constructed using coaxial loops mounted perpendicular to the solenoid axis of revolution. We then determined that the magnetic field uniformity within the solenoid could be vastly improved by first adjusting the number of turns, and then the position, of a number of the outer loops. Once the solenoid was designed and constructed, the solenoid scale factor, the magnetic field produced per ampere, was determined by applying a low frequency sine wave to separate the solenoid field from the background, and by measuring the magnitude of the field using a scalar magnetometer.

The unaligned and uncalibrated, collocated accelerometer and magnetometer sensor pair were then placed in the solenoid at a variety of orientations, and the calibration coefficients determined based on the magnitude of the magnetic and gravitational fields so that the precise positions and orientations of the sensors in the fields are not required. The alignment angles between the magnetometer and accelerometer are determined making use of the fact the solenoid's magnetic field is also horizontal, and therefore perpendicular to gravity.

2. Solenoid design

2.1 The infinite solenoid

To create uniform magnetic fields to test and calibrate sensors, researchers and manufacturers typically use a solenoid coil configuration where many turns are used as an approximation to an infinite solenoid. For the infinite solenoid, with some uniform turns per unit length denoted as n (measured in turns/m), the magnetic field everywhere inside the solenoid is parallel to the solenoid axis and is given as

$$B_\infty = \mu_o n I, \tag{1}$$

where μ_o is the magnetic permeability of free space and I is the current. For a practical solenoid, of some finite length L, the turns per unit length can be estimated as the total number of turns N divided by the solenoid length

$$n = \frac{N}{L}. \tag{2}$$

Due to the finite length and winding distribution of any realizable solenoid, however, the magnetic field inside will not be perfect and will deviate from B_∞, throughout the volume of the solenoid.

2.2 Practical solenoids

To investigate the magnetic field produced by a real solenoid it is possible to use the Biot-Savart law and to integrate over the current path to compute the magnetic field. In practise, the wire path can be divided up into small segments and the contribution from each segment summed to compute the overall magnetic field. The solution of an arbitrarily located straight line current segment is provided in Annex A, and can

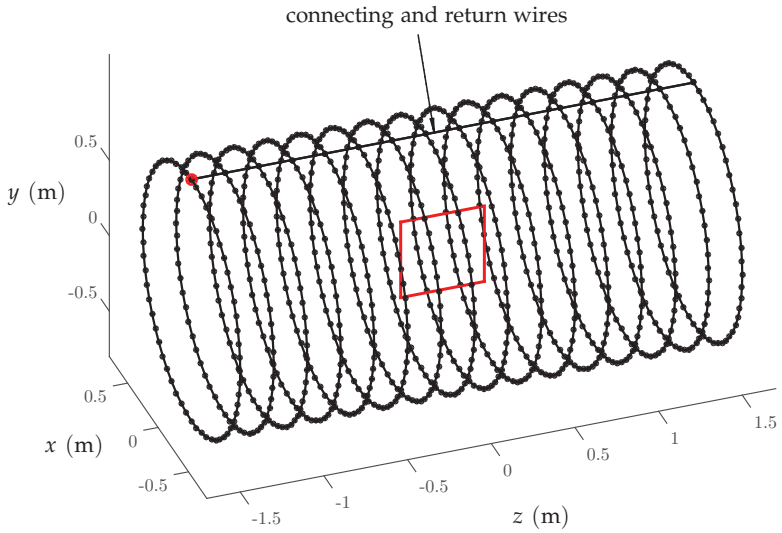

Figure 1: *Solenoid of coaxial loops formed from continuous segments of wire returning to start position.*

be utilized to develop a routine which accepts an array of $M+1$ points $\{(x_i, y_i, z_i), i = 1 \ldots M+1\}$, and computes the resulting magnetic field from the M segments.

Attempting to design a solenoid where the windings are laid using a constant pitch and then including a return wire to make the solenoid realizable, it is quickly discovered that unless the solenoid is excessively long the winding pitch will produce a field that deviates appreciably from the ideal solenoid. Further investigation leads to the conclusion that for a realizable and finite length solenoid the best uniformity is achieved when the windings form coaxial loops, with each of the connecting wires between the loops being cancelled out by a return wire as shown in Fig. 1.

Interestingly, it turns out, techniques exist for generating uniform magnetic fields that are **perpendicular** to the solenoid axis of revolution by using an infinitely long "$\cos(\theta)$ coil", where the current on the surface is proportional to the cosine of the angle of revolution [2]. Realizable versions of such coils are discussed in [3, 4].

Returning to solenoids formed using coaxial loops with a generated field **parallel** to the solenoid axis of revolution, in [5], the authors investigate the uniformity of; Helmholtz (two loops), Merrit (three or four loops) and Ruben (five loops) systems using finite element simulations, and conclude that the systems with more coils provide better uniformity. And, in [6] the magnetic field uniformity is improved by using smaller outer loops to increase the magnetic field levels near the solenoid ends.

We next introduce a definition for magnetic field uniformity and investigate the field uniformity versus solenoid length where the turns per unit length is uniform. We then introduce a two part optimization procedure to improve the magnetic field uniformity over a defined volume at the center of the solenoid by (1) optimizing the turns in a number of the outer loops as a real valued function, and (2) using the integer portion of the turns just determined, re-optimize the field by allowing the same outer loop positions to vary.

2.3 Magnetic field uniformity

Working in a rectangular coordinate system (x, y, z) and assuming that the solenoid is composed of coaxial loops whose axis of revolution is the z–axis, the magnetic field at the center of the solenoid will be parallel to the axis of revolution, and is defined as

$$\boldsymbol{B}_o = B_o \boldsymbol{a}_z \,, \tag{3}$$

where B_o is the magnitude of the magnetic field at the solenoid's center and $\boldsymbol{a}_z$ is the unit vector in the z–direction. In general, however, the magnetic field produced by the solenoid throughout its entire volume, defined here as $\boldsymbol{B}_a$ to recognize it as the applied field, will have components in all three directions such that

$$\boldsymbol{B}_a = \boldsymbol{a}_x \, B_{ax} + \boldsymbol{a}_y \, B_{ay} + \boldsymbol{a}_z \, B_{az}, \tag{4}$$

where $\boldsymbol{a}_x$ and $\boldsymbol{a}_y$ are the units vectors in the x and y–directions. The difference between the solenoid field at a position in the volume and the value at the center is defined as $\boldsymbol{B}_d$, and is given as

$$\boldsymbol{B}_d = \boldsymbol{a}_x \, B_{ax} + \boldsymbol{a}_y \, B_{ay} + \boldsymbol{a}_z \, \left(B_{az} - B_o\right). \tag{5}$$

We now introduce the *magnetic field uniformity* β defined as the ratio of the magnitude of the difference field divided by the center field[1] such that

$$\beta \equiv \frac{B_d}{B_o} = \frac{\left[B_{ax}^2 + B_{ay}^2 + \left(B_{az} - B_o\right)^2\right]^{1/2}}{B_o}. \tag{6}$$

Note that the magnetic field uniformity will have a non-zero value whenever the magnitude or direction of the solenoid's magnetic field differs from the center value, and that by definition β will equal zero at the solenoid center. For the hypothetical infinite solenoid where the magnetic field is constant and parallel to the solenoid axis, β equals zero everywhere inside the solenoid. Our goal is to create a finite length solenoid that achieves a highly uniform magnetic field at the solenoid center region.

2.4 Finite length solenoids with uniform turns per unit length

The initial design stage, and original work, was conducted using small current segments to represent the solenoid, and it was found that as smaller and smaller segments were used, representing arc lengths of 5°, 2° and 1°, that numerical error was becoming significant in the final result. Therefore, the design work proceeded by computing the solenoid's magnetic field by summing the contribution from a number of coaxial loops, using the analytical solution provided for a single current loop given in Annex B. In the discussions that follow we adapt the terminology that a loop is composed of a number of turns at each position along the solenoid axis.

To approximate the infinite solenoid, a somewhat intuitive approach would call for equally spaced coaxial loops, each with an equal number turns. To get a sense of how the magnetic field uniformity of such a solenoid varies with length, we computed the magnetic field for increasingly larger solenoids with loops spaced every 20 cm along the axis, each with a radius of 0.8 m. The solenoid shown in Fig. 1 represents the case where sixteen loops are used, and the solenoid is 3.0 m in length.

To achieve a representative number for the uniformity as the length increases we computed the magnetic field uniformity β over a 50 cm by 50 cm grid with 1 cm spacing at the center of the solenoid, as represented

[1] In [3] the magnetic field uniformity is defined using the difference of the magnitudes of the solenoid field and the center field, instead of the magnitude of the difference vector as used here.

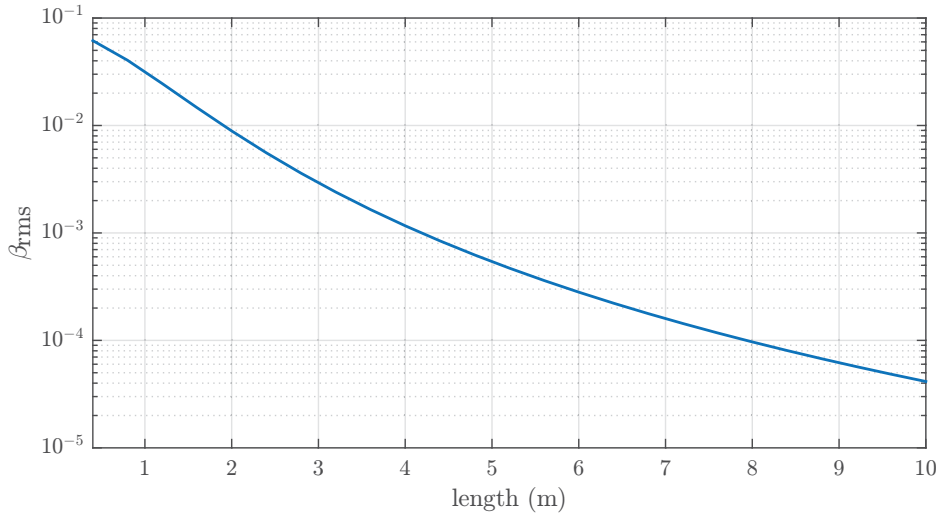

Figure 2: *Magnetic field uniformity versus solenoid length.*

by the red square in Fig. 1. We then computed the rms (root mean square) value of the uniformity on this grid, such that

$$\beta_{\mathrm{rms}} = \left(\frac{1}{P} \sum_{i,j} \left| \beta \left(x_i, z_j \right) \right|^2 \right)^{1/2}, \tag{7}$$

where P is the total number of points on the grid, and x_i and z_j are the grid locations. The results of these calculations for solenoids up to a length 10 m are shown in Fig. 2, from which it is observed that a 3 m solenoid achieves a magnetic field uniformity β_{rms} value of about 3×10^{-3}.

Nominally our overall design goal would be to achieve better than 1 % accuracy for the underwater magnetic signature measurements, corresponding to magnetic field uniformity rms levels of about 10^{-3}. Noting, however, that the uniformity over the grid can be two to five times larger than the rms level, an rms level nearing better than 10^{-4} is necessary. Referring to Fig. 2 again, uniformities of less than 10^{-4} are only achieved for this particular example, when the length approaches 8 m.

2.5 Improving solenoid uniformity

On closer inspection of the magnetic uniformity of the 16 loop example shown in Fig. 3, with a uniform turns per unit length, we observe as shown in Fig. 3a that the field uniformity rapidly degrades away from the solenoid center and actually approaches unity near the ends of the solenoid. This occurs because the magnetic field near the ends of the solenoid is decreasing as well as diverging, as the field outside the solenoid takes on the form of a magnetic dipole. Also shown in Fig. 3a is the grid used to compute the rms values of β which were plotted in Fig. 2, and which will be used as the grid over which the magnetic field uniformity will be improved.

To improve the uniformity near the solenoid center we set up an optimization problem where the mean square value of the magnitude of the difference field B_d from Eqn. (5), computed on the same 50 cm by 50 cm grid used above, is minimized by allowing the number of turns in the outer three coils at both ends of the solenoid to vary as real-valued continuous variables as is required for optimization problems. This would represent a somewhat fictitious case where the outer loops would be powered by separate power

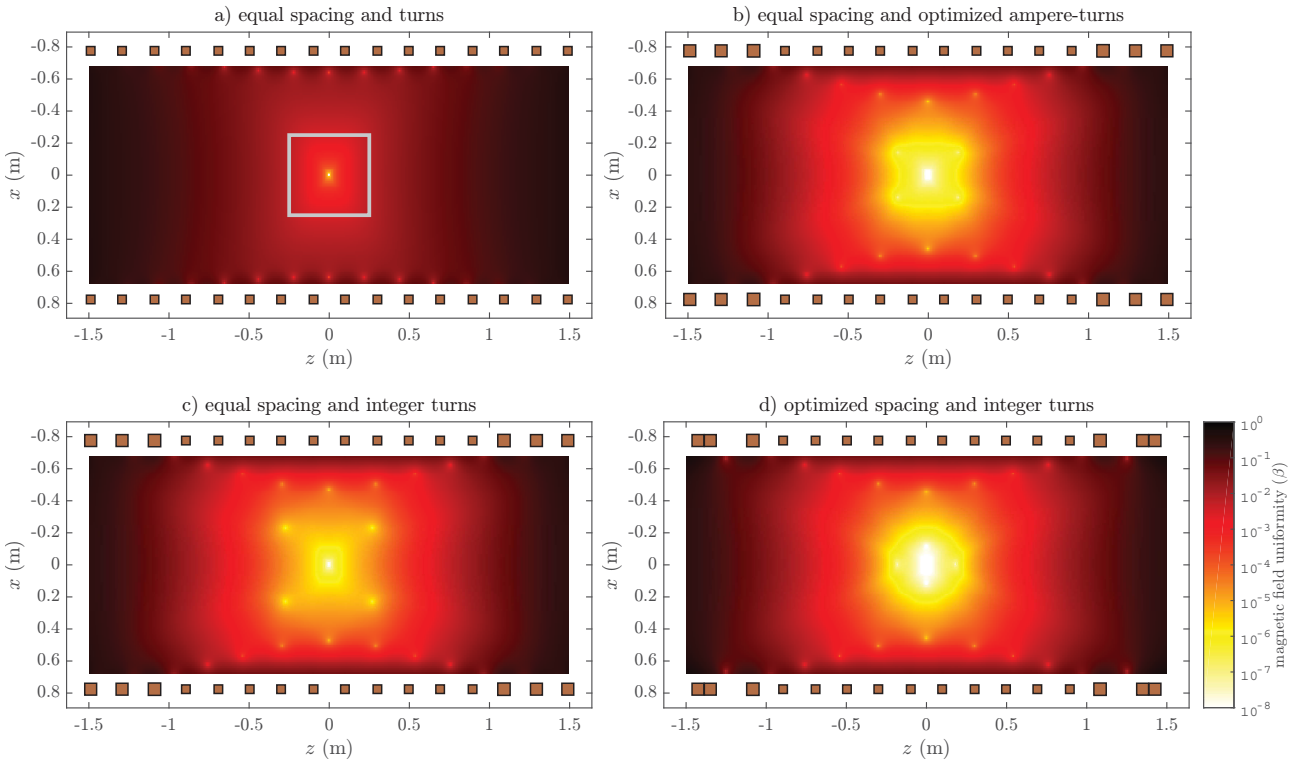

Figure 3: *Magnetic field uniformity demonstrating solenoid design procedure. a) equal turns and spacing. b) equal spacing and optimized ampere-turns. c) equal spacing and integer turns. d) optimized spacing and integer turns. The loop positions are shown as squares proportional to the number of turns.*

supplies and is referred to as the optimized ampere-turns case.

To achieve a center magnetic field value B_o of about 100 µT with a current of 1 A, the initial design set the number of turns to 18. For the actual solenoid build the length of the solenoid (or more precisely the initial distance between the outer loops) was shortened to 2.98 m and the effective radius was determined to be 0.7769 m. To apply the copper wire windings, sixteen precise channel rings were fabricated using PVC strips of equal length which were glued and shimmed to keep the loops coaxial as measured by a laser level. The effective radius is meant to represent the center of each loop and takes into account the fibreglass cylinder, the PVC strips, and the number of layers used to wind the turns. To keep the winding area as small as possible, 22AWG copper wire with very thin PVC insulation was laid in layers of 5 turns. The entire solenoid required just over 1600 m of wire, weighing 4.8 kg with about 81 Ω of resistance. Fig. 4 shows a photograph of the constructed solenoid with the PVC rings and copper wire windings in place.

The optimization procedure was implemented using the `fmincon` routine within MATLAB's Optimization Toolbox [7], and determined values of 25.01 turns, 24.94 turns and 26.06 turns for the three outer loops. The field uniformity for these ampere-turn values is shown in Fig. 3b, where field uniformities of less than 10^{-6} have been created over the grid.

To create a more realizable design, one using a single power supply with a continuous winding, the number of turns is rounded to the nearest integer and the mean square value of the magnitude of the difference field B_d is re-optimized by allowing the position of the same outer three loops to vary. As seen in Fig. 3c some loss of uniformity occurs when the integer portion of the number of turns is used with

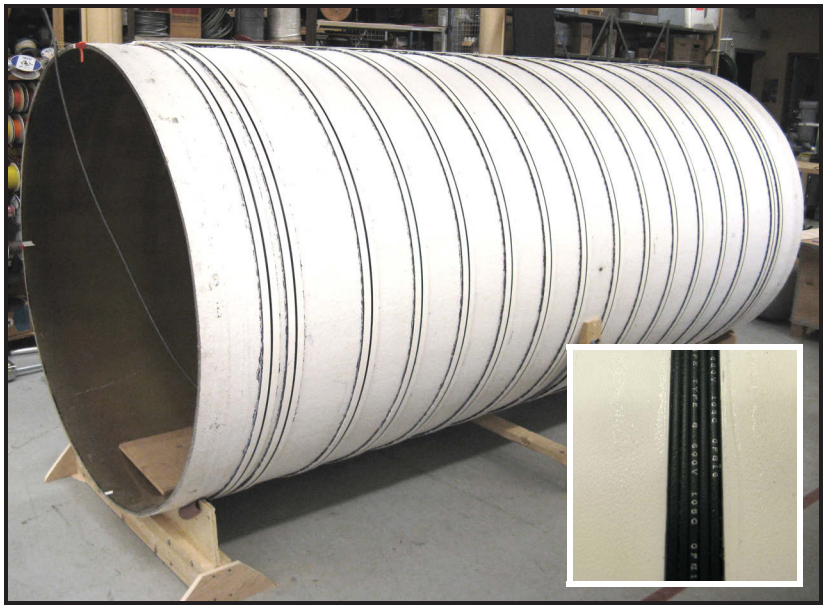

Figure 4: *Constructed solenoid, with the PVC bands and windings in place. Inset photo shows zoom of copper windings laid in the PVC channel.*

equal spacing. For the re-optimization of the field the location of the three coils is constrained to be plus or minus half a loop spacing to avoid loops swapping position. The loop offsets determined to re-optimize the uniformity, were $+6.32\,\text{cm}$, $-5.54\,\text{cm}$ and $+0.66\,\text{cm}$, and the resulting field uniformity is shown in Fig. 3d.

The solenoid's center field per unit current, the (nT/A) factor of the solenoid, is defined as K, and changes at each design stage as the number of turns and coil positions are varied. The calculated values in the design order are $102\,338\,\text{nT/A}$, $107\,530\,\text{nT/A}$, $107\,521\,\text{nT/A}$ and $107\,551\,\text{nT/A}$. As only the final design is constructed, it is the last value in the list which is of interest.

An extensive study on how the number of loops, turns, solenoid geometry, optimization grid, and number of outer loops to adjust, affects the final results has **not** been conducted, and the solutions presented here likely do not represent a global minimum but are instead one set of a number of possible solutions.

2.6 Solenoid calibration

To calibrate the solenoid we are interested in establishing the solenoid's scale factor, that is, the amount of field produced at the center per unit current. Two simultaneous measurements are therefore required, the magnitude of the center magnetic field and the current used to produce that magnetic field.

2.6.1 Solenoid scalar magnetometer measurements

To measure the magnitude of the center magnetic field a Geometrics G-824A Cesium Magnetometer [8] was used. A scalar magnetometer is preferred for this measurement since its field reading is independent of the sensor orientation, provided the magnetic field remains within the $\pm 30^\circ$ cone of operation of the G-824A. The Geometrics G-824A also possesses excellent specifications with an absolute sensor accuracy of $< 3\,\text{nT}$ and a noise floor of $0.3\,\text{pT}/\sqrt{\text{Hz}}$, and due to its advanced counter technology is capable of sampling rates up to 1000 Hz. For our testing the sample rate was set at 250 Hz.

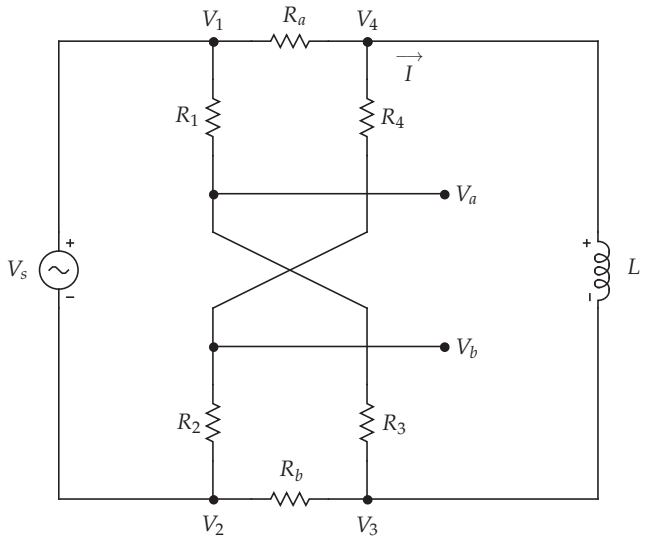

Figure 5: *Newly developed differential current monitoring circuit. Regardless of the resistor values the output voltage V_{ab} is directly proportional to the load current I, with no common mode signal created. The input voltage is represented by the sine source V_s and the solenoid is represented by the inductor L.*

2.6.2 Solenoid current measurements

To create a voltage proportional to the applied current with the required accuracy and minimal drift, we developed a novel differential current monitoring circuit as depicted in Fig. 5. A detailed analysis of the circuit with general valued resistors, reveals that the differential voltage across the output terminals *a* and *b*, defined as $V_{ab} = V_a - V_b$, is directly proportional to the load current with zero common mode signal introduced, regardless of the resistors values. This feature vastly improves the common mode rejection ratio compared to current monitoring techniques using a single shunt resistor.

A simplified analysis of the differential current monitor can be performed by setting $R_1 = R_2 = R_3 = R_4$, and $R_a = R_b$, to determine an approximation for the output voltage, V_{ab} as

$$V_{ab} = \frac{2R_1 + R_s}{2R_1 - R_a} R_a \, I, \tag{8}$$

where R_s is the solenoid resistance and I is the solenoid current. When $R_1 \gg R_a$ and R_s, the output voltage simplifies to $V_{ab} = R_a I$.

To improve the temperature stability of the differential current monitor gain; a 10 kΩ resistor four pack, such as that described [9] with better than ±5 ppm/°C temperature tracking rating was used for resistors R_1 through R_4. Resistors R_a and R_b were hand selected and measured to be well matched.

2.6.3 Long-term solenoid scale factor measurements

Any magnetic field measurement made within the solenoid will be the sum of the field produced by the solenoid, and that due to external influences outside of the solenoid. The total vector field near the center of the solenoid, defined as $\boldsymbol{B}_t$, is then the sum of the field produced by the solenoid $\boldsymbol{B}_a$, which is now assumed to have only a *z*–axis component, and an external field $\boldsymbol{B}_e$ which has components in all three directions, hence

$$\boldsymbol{B}_t = B_{ex}\boldsymbol{a}_x + B_{ey}\boldsymbol{a}_y + \left(B_a\left(t\right) + B_{ez}\right)\boldsymbol{a}_z \, . \tag{9}$$

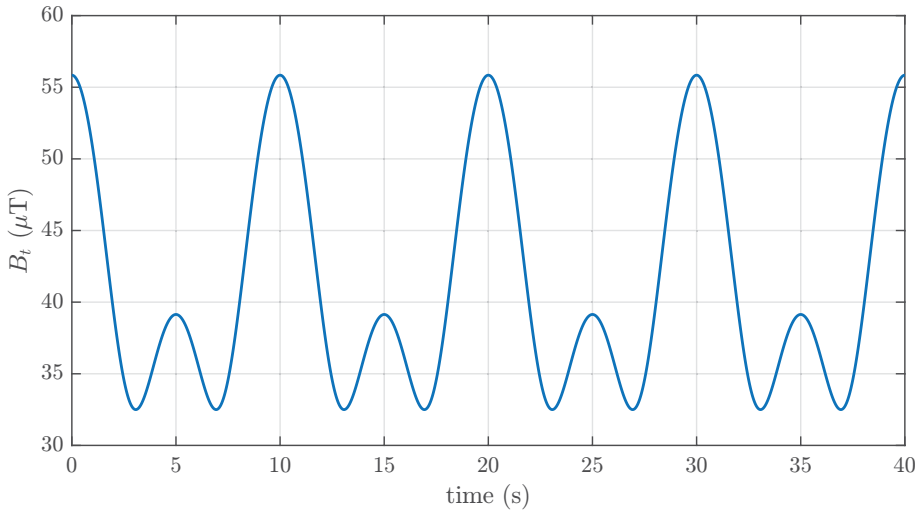

Figure 6: *Example of the total field inside the solenoid when a sinusoidal field is applied. This example, typical for the measurements conducted, shows B_t when the solenoid current is a* 0.1 Hz *sine wave, with* B_a =33.6 µT,B_{ez} =11.8 µT, *and* B_{er} =32.5 µT.

The magnitude of this field can be expressed as

$$B_t = \left[B_{er}^2 + \left(B_a\left(t\right) + B_{ez}\right)^2\right]^{1/2}, \tag{10}$$

where B_{er} is the radial component of the external field such that $B_{er}^2 = B_{ex}^2 + B_{ey}^2$, and is perpendicular to the solenoid axis.

The magnetic field produced by the solenoid is directly proportional to the current, such that $B_a\left(t\right) = K\, I\left(t\right)$. If the solenoid current is sinusoidal and of sufficient strength that the field produced is greater than B_{ez}, then the magnitude of the field within the solenoid B_t will be similar in structure to that shown in Fig. 6. As the current varies sinusoidally, there are three specific values worth identifying. Firstly, B_t is at its minimum, B_{er}, when $B_a = -B_{ez}$. Secondly, B_t reaches its maximum when B_a is maximum in the direction of B_{ez}. Thirdly, the secondary maximum in B_t occurs when B_a peaks in the direction opposing B_{ez}.

Since our concern is with frequencies below 1 kHz and ultimately with determining the calibration coefficients to be introduced in the next section, in order to separate the applied field from the quasi-stationary background magnetic fields we use a test frequency of 0.1 Hz for the applied current. At this frequency the applied current and the field produced will be in phase, as will the current and voltage of the solenoid as the coil inductance is negligible at such a low frequency.

With the scalar magnetometer at the solenoid center we applied an approximately ±0.6 A sine wave with a 0.1 Hz frequency to the solenoid, for a period of about 12 days, and every 10 minutes measured ten oscillations of the field and current. For each of those measurements a least squares procedure determined estimates of the solenoid scale factor K, and the components of the external field, parallel and perpendicular to the solenoid, B_{ez} and B_{er}, respectively. The estimates of the solenoid scale factor are shown in Fig. 7 for those measurements where the fitting error was less than 2 nT. Plots of the B_{ez} and B_{er} estimates are not shown but are roughly consistent with the earth's magnetic field in those directions for the locale. Some of the B_{ez} and B_{er} estimates while constant over the two minute measurement interval, vary significantly due to the presence of stationary magnetic object for some period of time. Of note, is that while significant changes in B_{ez} and B_{er} were observed, the estimated solenoid scale factor was very stable. The average

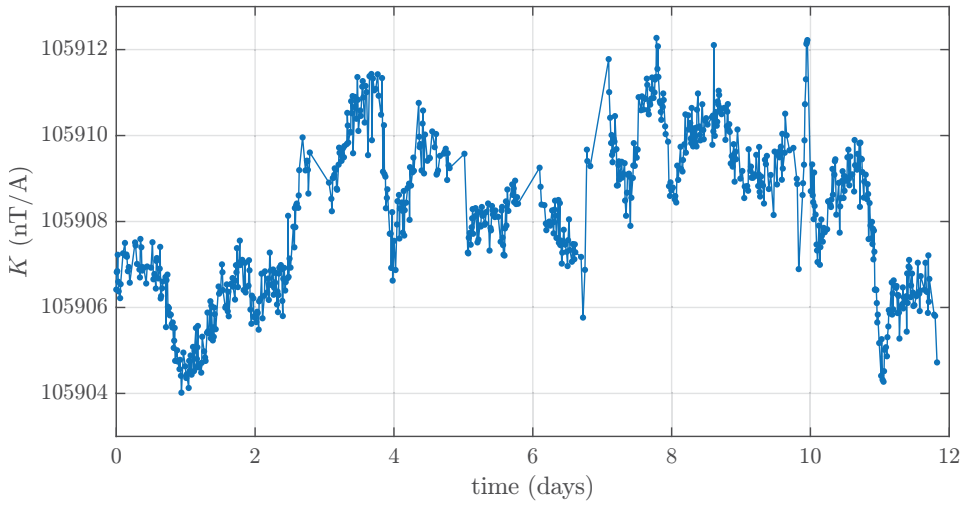

Figure 7: *Solenoid scale factor K repeatedly measured Nov 1–12, 2014. Mean value of* 105 908 nT/A *with a standard deviation of* 1.81 nT/A.

scale factor over the time period was found to be 105 908 nT/A with a standard deviation of just 1.81 nT/A, so that the ratio of the standard deviation to the measured value was smaller than 2×10^{-5}.

The current monitor's data acquisition system operates independent of the scalar magnetometer data acquisition system so some measurements failed to fit accurately due to drift between the sampling rates. The more common occurrence was the presence of an anomaly which caused the measurement to be rejected. Future work will involve improving the synchronization of the scalar magnetometer and current monitor data acquisition systems.

Comparison of the calculated solenoid scale factor 107 551 nT/A, and the measured scale factor 105 908 nT/A shows a difference of about 1.5 %. This difference arises due to the fact that in its present configuration the current monitor is installed directly between the power amplifier and the solenoid, and the relationship given in Eqn. (8) does not take into account the loading of the circuit. It is also difficult to directly measure this loading effect due to the relatively high impedance and voltage levels of the circuit. However, what is critical moving forward to calibrate the magnetometers is that the same voltage is measured for a given field, and this condition does exist, since the passive loading remains fixed. In addition to better synchronizing the current monitor's data acquisition system, an active version of the current monitor is to be developed to minimize the passive loading of the circuit and to better match the result in Eqn. (8).

In addition to the long term measurements of the solenoid scale factor at the solenoid center, a series of similar measurements were made on a 60 cm by 60 cm grid at 10 cm intervals, near the solenoid center, and the scale factor was found to be consistent, throughout the grid, to measurement accuracy.

3. Magnetometer and accelerometer calibration and alignment

With the ability to produce a uniform magnetic field over a large volume it was now possible to apply a known magnetic field to a device under test, based on the measurement of the electrical current. In addition to being uniform, careful attention was taken to keep the loops vertical so that the uniform field would also be horizontal which is critical to determining the alignment angles. To calibrate and

align a collocated three-axis accelerometer and three-axis magnetometer sensor pair we first introduce calibration and alignment models for the magnetometer and accelerometer, and then provide detail on the data collection and processing procedure to determine their values.

The sensors under test are represented in the cut away diagram of a magnetic node in Fig. 8 and include a Bartington MAG-03 three-axis magnetometer [10] mounted below the data acquisition circuit board which includes an Analog Devices ADXL327 three-axis $\pm 2\,\mathrm{g}$ accelerometer integrated circuit [11]. During assembly the axes of the magnetometer and accelerometer are only nominally aligned. The magnetic nodes also include depth and temperature sensors. Data transfer from each node, which includes the three-axis magnetometer, three-axis accelerometer, depth and temperature values, is done using a high-speed, time division multiplexed data transfer protocol. Each node connects in parallel to a data bus comprised of only a power pair, a sample pair and a data pair; dramatically reducing the amount of copper and connectors compared to traditional star-configured data acquisition systems [12].

The magnetic node sensors have been developed by DRDC in conjunction with Omnitech Electronics as part of the Transportable Underwater Range for Naval Signatures (TURNS) project to provide the Royal Canadian Navy with a portable magnetic ranging capability in support of the Halifax Class Modernization.

The calibration and alignment procedure is done in three stages, (1) calibration of the accelerometer, (2) calibration of the magnetometer, and (3) alignment of the magnetometer to the accelerometer. The mathematical models required for each of the three stages are presented next. To avoid introducing additional sets of axes for the magnetometer and accelerometer, we reuse the conventional (x, y, z) for each, and will also introduce a *goes to* operation, represented by a long left arrow ($\Leftarrow$), to avoid additional subscripted variables.

3.1 Magnetometer calibration model

A three axis magnetometer such as the MAG-03 is constructed as three separate analog sensors measuring the field components along three near-orthogonal directions, defined as $\left(B_x, B_y, B_z\right)$, and can be assumed to be nominally scaled to Tesla (T). Since the three outputs are analog signals, each will have a scale and offset error associated with it. These errors in the analog signals can be corrected by scaling and offsetting the output channels, such that

$$\begin{bmatrix} B_x \\ B_y \\ B_z \end{bmatrix} \Leftarrow \begin{bmatrix} k_x & 0 & 0 \\ 0 & k_y & 0 \\ 0 & 0 & k_z \end{bmatrix} \begin{bmatrix} B_x \\ B_y \\ B_z \end{bmatrix} + \begin{bmatrix} d_x \\ d_y \\ d_z \end{bmatrix}, \tag{11}$$

which can also be expressed using matrix notation as

$$\boldsymbol{B} \Leftarrow \boldsymbol{k}\boldsymbol{B} + \boldsymbol{d}, \tag{12}$$

where $\boldsymbol{B}$ is the magnetic field vector, $\boldsymbol{k}$ is a diagonal scale matrix, and $\boldsymbol{d}$ is the offset correction vector.

The three magnetic field values will also have errors due to misalignment of the axes, which can be corrected to a true orthogonal set of axes using an orthogonality correction matrix [1]. The orthogonality correction matrix is a function of three angles, the first angle α_m corrects the y–axis to be orthogonal to the x–axis, the remaining two angles, defined as β_m and γ_m, correct the z–axis to be orthogonal to both the x and y axes. In terms of the magnetic field components, the orthogonality correction relationship is given as

$$\begin{bmatrix} B_x \\ B_y \\ B_z \end{bmatrix} \Leftarrow \begin{bmatrix} 1 & 0 & 0 \\ \cos\alpha_m & \sin\alpha_m & 0 \\ \cos\gamma_m & \cos\beta_m & \left(1 - \cos^2\beta_m - \cos^2\gamma_m\right)^{1/2} \end{bmatrix}^{-1} \begin{bmatrix} B_x \\ B_y \\ B_z \end{bmatrix}, \tag{13}$$

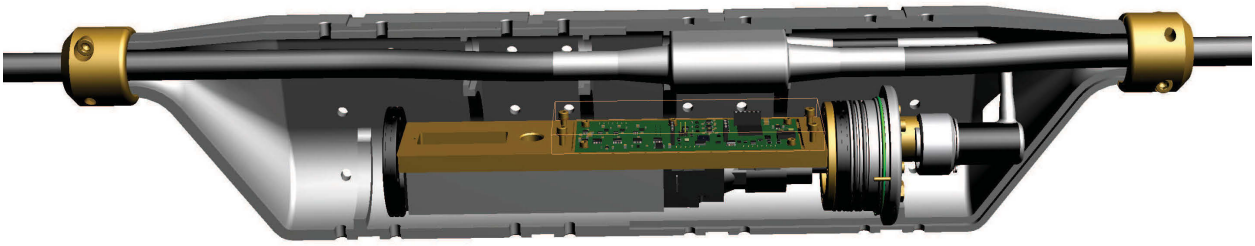

Figure 8: *Three dimensional representation of a magnetic node with collocated three axis magnetometer and accelerometer sensors.*

and is applied after the scale and offset corrections above. Eqn. (13) can be expressed using matrix notation as

$$\boldsymbol{B} \Leftarrow \boldsymbol{Q}\boldsymbol{B}, \tag{14}$$

where $\boldsymbol{Q}$ is defined as the orthogonality correction matrix, and requires the computation of a matrix inverse. In summary, the two magnetometer corrections can be combined and expressed as

$$\boldsymbol{B} \Leftarrow \boldsymbol{Q}\left(\boldsymbol{k}\boldsymbol{B} + \boldsymbol{d}\right). \tag{15}$$

If the magnetometer outputs require no calibration, all scale factors would equal unity, all offsets would equal zero, and all orthogonality correction angles would be 90°.

3.2 Accelerometer calibration model

Initially, for the three-axis accelerometer a similar set of corrections were applied to correct errors in the accelerometer output channels. However, the three-axis accelerometer used is manufactured on a single substrate, and as a result there exists some electrical crosstalk between the channels, so we adopted the full crosstalk model recommended by some manufacturers [13]. In this model the accelerometer outputs are represented as $\left(A_x, A_y, A_z\right)$, and are assumed to be nominally scaled relative to gravity, and are corrected as

$$\begin{bmatrix} A_x \\ A_y \\ A_z \end{bmatrix} \Leftarrow \begin{bmatrix} h_{xx} & h_{xy} & h_{xz} \\ h_{yx} & h_{yy} & h_{yz} \\ h_{zx} & h_{zy} & h_{zz} \end{bmatrix} \begin{bmatrix} A_x \\ A_y \\ A_z \end{bmatrix} + \begin{bmatrix} c_x \\ c_y \\ c_z \end{bmatrix}, \tag{16}$$

or more succinctly as

$$\boldsymbol{A} \Leftarrow \boldsymbol{h}\boldsymbol{A} + \boldsymbol{c}, \tag{17}$$

where $\boldsymbol{A}$ is the relative accelerometer vector[2], $\boldsymbol{h}$ is the crosstalk matrix, and $\boldsymbol{c}$ is the offset vector.

If the accelerometer outputs required no correction, the crosstalk matrix would equal an identity matrix (ones along the diagonal and zero off-diagonal values), and the offsets would equal zero.

3.3 Alignment model

The last step of the process is to align the now scaled and orthogonal axes of the magnetometer and accelerometer into a coincident axis system. While the alignment of the axes can be done in either direction, we choose to align the magnetometer axes to the accelerometer axes, since the magnetometer

[2]By convention, $\boldsymbol{A}$ is usually defined as the magnetic vector potential, but is used here to represent the relative acceleration vector.

data once aligned to the accelerometer can then be rotated to horizontal and vertical components using the accelerometer values.

There exists a number of methods to rotate data from one set of orthogonal axes to another set of orthogonal axes, we select the method often referred to as the yaw, pitch and roll method. The procedure begins by first rotating around the original x–axis by some angle defined here as ψ_x, then rotating around the new y–axis by some angle ϕ_y, and lastly, rotating around the final z–axis by some angle θ_z. Here ψ_x is defined as the roll, ϕ_y as the pitch, and θ_z as the yaw.

Mathematically these operations can be described as

$$\begin{bmatrix} B_x \\ B_y \\ B_z \end{bmatrix} \Leftarrow \boldsymbol{R}_z \boldsymbol{R}_y \boldsymbol{R}_x \begin{bmatrix} B_x \\ B_y \\ B_z \end{bmatrix}, \tag{18}$$

where the rotation matrices, $\boldsymbol{R}_x$, $\boldsymbol{R}_y$ and $\boldsymbol{R}_z$ are given as

$$\boldsymbol{R}_x = \begin{bmatrix} 1 & 0 & 0 \\ 0 & \cos\psi_x & \sin\psi_x \\ 0 & -\sin\psi_x & \cos\psi_x \end{bmatrix}, \tag{19}$$

$$\boldsymbol{R}_y = \begin{bmatrix} \cos\phi_y & 0 & -\sin\phi_y \\ 0 & 1 & 0 \\ \sin\phi_y & 0 & \cos\phi_y \end{bmatrix}, \tag{20}$$

and

$$\boldsymbol{R}_z = \begin{bmatrix} \cos\theta_z & \sin\theta_z & 0 \\ -\sin\theta_z & \cos\theta_z & 0 \\ 0 & 0 & 1 \end{bmatrix}, \tag{21}$$

respectively. Eqn. (18) can also be expressed using matrix notation as

$$\boldsymbol{B} \Leftarrow \boldsymbol{R}_z \boldsymbol{R}_y \boldsymbol{R}_x \boldsymbol{B}. \tag{22}$$

When no rotations are required all the rotation angles are zero, and the rotation matrices simplify to identity matrices.

3.4 Calibration and alignment procedure

The task at hand is to determine the best set of calibration and alignment values based on a series of measurements made with the collocated magnetometer and accelerometer located in a variety of orientations within the uniform field solenoid. To allow the magnetic nodes to be easily rotated to different positions a three-axis gimbal was constructed inside of the solenoid as shown in Fig. 9. The gimbal was specially designed so that the center of the magnetometer would remain close to the exact center of the solenoid regardless of the rotation. This was done in order to minimize the local magnetic field variation seen at the magnetometer sensors. The gimbal was also constructed primarily of wood using nonmagnetic fasteners. When referring to the positioning of the magnetic nodes within the solenoid, the gimbal is not accurately aligned within the solenoid. Each of the planes of the three-axis gimbal have small indexing holes that allow the surface to be rotated at 45° intervals, which are nominally aligned to the solenoid axis. In the processing that follows the fitting function always involves the magnitude of the fields and this avoids having to accurately orientate the magnetic nodes within the solenoid. Having to align the magnetic nodes

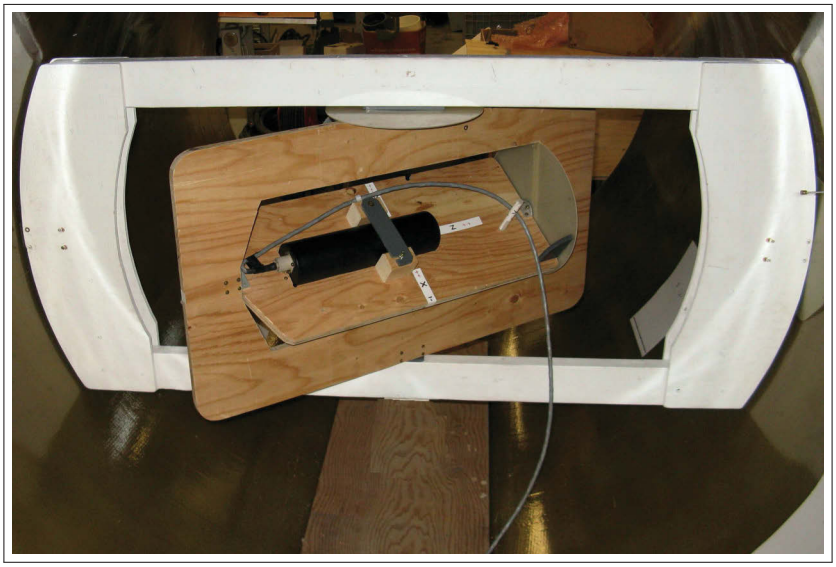

Figure 9: *Three axis gimbal mounted in the center of the uniform field solenoid.*

accurately in the solenoid would actually render the process near impossible, keeping in mind that the sensors are housed within a pressure vessel that is inside another pressure vessel, as seen in Fig. 8.

The procedure to determine the calibration and alignment values of a magnetic node evolved through a series of tests. For all the measurements, however, the magnetic node under test was locked into the gimbal and, as was done for the solenoid calibration, ten oscillations of the applied field were recorded. As the accelerometer is stationary, each of the accelerometer readings were basically constant, while the magnetic field readings were essentially a sine wave with an offset.

The first set of measurements used to determine the calibration and alignment values were composed of measurements where the positive and negative direction of each of the principal axes was aligned to the applied magnetic field, and the sensor rotated by four 90° rotations about these axes, for a total of 24 measurements. In this configuration all the applied magnetic field would be observed primarily along a single axis, and the gravitational field would be observed primarily on another axis. The second set of measurements was essentially a repeat but with the sensor tilted forward 45°, so that two of the axes would observe $\sqrt{2}/2$ of the applied magnetic field and the gravitational field. The results revealed much better convergence for the orientations where the fields were being observed on two axes.

Expanding on the concept that maximizing the field strength on as many axes as possible for each measurement, we observed that if two 45° rotations are performed about any two axes, one channel will measure $\sqrt{2}/2$ of the field, while the other two channels measure $1/2$ of the field. For example, if a magnetometer started with its axes aligned to the solenoid in Fig. 1, a $\pm 45°$ (or $\pm 135°$) rotation about the x–axis, followed by $\pm 45°$ (or $\pm 135°$) rotation about the z–axis, will make the z–component for both the gravity and magnetic fields $\sqrt{2}/2$, and the remaining values $1/2$. This example yields 16 measurements and is dominant in the z–component because the z–axis starts aligned with the solenoid axis. Similar rotations can be applied so that the x–component, and then the y–component, have the large field value. In total the double 45° rotation approach provides 48 separate measurements. The calibration results for these data sets were observed to provide the best convergence and was chosen as the preferred method.

Parts of the analysis presented were done using the IDL programming language [14], as well as NI LabVIEW [15] for the development of a real-time application. The constrained minimization results

obtained using these programs were consistent with the results using MATLAB.

3.4.1 Accelerometer calibration procedure

Ignoring local variations in the earth's gravitational field, which are reported to vary by up to 1 %, the magnitude of the relative acceleration vector should equal one in any orientation. As a result the least squares cost function, defined as Ψ_a takes the form

$$\Psi_a = \sum_{i=1}^{N} (1 - A_i)^2 , \tag{23}$$

where N is the number of measurements and A_i is the magnitude of the corrected relative gravity vector, from Eqn. (16), and is calculated as

$$A_i = |\boldsymbol{A}_i| = (\boldsymbol{A}_i \cdot \boldsymbol{A}_i)^{1/2} . \tag{24}$$

where $\boldsymbol{A}_i \cdot \boldsymbol{A}_i$ is the dot or inner product, and equals $\boldsymbol{A}_i^t \boldsymbol{A}_i$ where $[\,]^t$ is the vector transpose. Fitting results are compared using the root mean square error defined as $\sigma_a = (\Psi_a / N)^{1/2}$.

Presented in Fig. 10 is an accelerometer calibration example for a magnetic node under development. The crosstalk matrix $\boldsymbol{h}$ and offsets $\boldsymbol{c}$ determined to minimize the cost function were

$$\boldsymbol{h} = \begin{bmatrix} 0.99242 & -0.00058 & 0.00892 \\ 0.00177 & 1.03733 & -0.00109 \\ 0.00890 & 0.00081 & 0.98987 \end{bmatrix}, \qquad \boldsymbol{c} = \begin{bmatrix} -0.06604 \\ 0.18185 \\ 0.04931 \end{bmatrix},$$

respectively, and reduced the rms error by a factor of 152 from 11.0 % to 0.072 %.

According to specifications, the ADXL327 scale factors can vary by up to 10 % of the typical value, while the offsets can be up to 50 % of gravity. The quoted crosstalk factors are less than 1 %. Therefore the values determined all within specification. While the scale factors are highly stable with temperature changes, the offset values, can vary by up to 2 % for a 10 °C change, and would need to be accounted for if significant temperature changes from the calibration temperature are expected.

Prior to the calibration the accelerometer had undergone no calibration whatsoever and for this reason the pre-calibration errors are excessively large. Once calibrated however the error is quite small and better than our design goal. Table 1 lists the error before and after calibration for the accelerometer, along with the errors for the magnetometer and alignment which are discussed next. In Section 3.5 a first order error analysis is performed to provide an estimate of the total error.

3.4.2 Magnetometer calibration procedure

When a three-axis magnetometer is placed within the solenoid and a current applied, the magnetic field components measured by the magnetometer, assuming any external field is stationary over the observation time, will be some multiple of the applied field plus a constant, such that the magnetometer field components can be expressed as

$$B_x(t) = m_x B_a(t) + b_x, \tag{25}$$
$$B_y(t) = m_y B_a(t) + b_y, \tag{26}$$
$$B_z(t) = m_z B_a(t) + b_z. \tag{27}$$

The magnitude of the magnetic field defined as B_t, is the square root of the sum of the squares of the components, such that

$$B_t = \left[B_x^2(t) + B_y^2(t) + B_z^2(t) \right]^{1/2}, \tag{28}$$

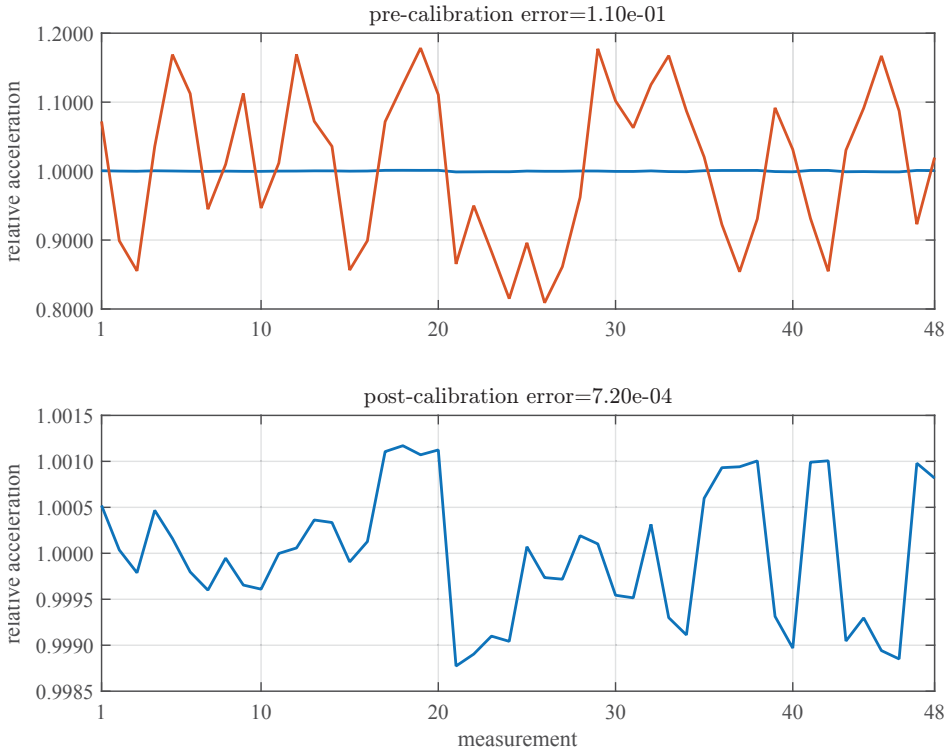

Figure 10: *Accelerometer calibration example: top traces are the relative acceleration magnitudes before (red) and after (blue) calibration, while the bottom trace shows only the after calibration result.*

and can now be expressed as

$$B_t = \left[(\boldsymbol{m} \cdot \boldsymbol{m})\, B_a^2(t) + 2\,(\boldsymbol{m} \cdot \boldsymbol{b})\, B_a(t) + (\boldsymbol{b} \cdot \boldsymbol{b}) \right]^{1/2}, \tag{29}$$

where the magnetic field component multiplier and offset vectors are defined as

$$\boldsymbol{m} = \begin{bmatrix} m_x & m_y & m_z \end{bmatrix}^t, \tag{30}$$

and

$$\boldsymbol{b} = \begin{bmatrix} b_x & b_y & b_z \end{bmatrix}^t, \tag{31}$$

respectively. The magnetic field component multiplier vector can also be referred to as the relative applied magnetic field.

On rearranging Eqn. (10), the magnitude of the magnetic field in solenoid coordinates, can be written as

$$B_t = \left[B_a^2(t) + 2 B_{ez} B_a(t) + B_e^2 \right]^{1/2}, \tag{32}$$

where B_e is the magnitude of the external field and given as $B_e^2 = B_{ex}^2 + B_{ey}^2 + B_{ez}^2$. Since the magnitude of the field must be the same in either coordinate system, the coefficients in Eqns. (29) and (32), can be equated to yield

$$\boldsymbol{m} \cdot \boldsymbol{m} = 1, \tag{33}$$

$$\boldsymbol{m} \cdot \boldsymbol{b} = B_{ez}, \tag{34}$$

$$\boldsymbol{b} \cdot \boldsymbol{b} = B_e^2. \tag{35}$$

Thus, the magnitudes of the alternating and constant components in each coordinate system must be equal, and by using Eqn. (34) the external magnetic field along the solenoid axis, B_{ez}, can be determined as the dot product of $\boldsymbol{m}$ and $\boldsymbol{b}$. This is an interesting result since the orientation of the magnetometer is arbitrary with respect to the solenoid. Determining a cost function for the magnetometer measurements is not as straightforward as for the accelerometer, as it is not possible to simultaneously satisfy Eqns. (33,34,35) as a single cost function.

Our first approach was to work entirely in the time domain and to minimize the difference of the magnitude computed using Eqn. (28) and Eqn. (32), and initially, the model included a single estimate for B_{ez} and B_e used to compensate all measurements. This approach provided reasonable scale and orthogonality corrections but the magnetometer offset corrections were in the hundreds of nano-Teslas (nT). The next stage was to parameterize the field components according to Eqns. (25,26,27) and then estimate B_{ez} and B_e for each measurement. This approach yielded the same scale and orthogonality corrections as the first approach but the magnetometer offset corrections were now in the tens of nT.

The MAG-03 magnetometer offset error, as provided in [10], is quoted as less than 5 nT, so it was clear our estimates were due not only to changes in the external field in time, but due to the slight differences in positions, estimated to be less than 2 cm, in a large gradient field.

What we also determined, however, was that the same scale and orthogonality corrections could be determined by just using Eqn. (33) alone, which leads to essentially the same cost function used for the accelerometer in Eqn. (36), but replacing A_i with m_i. We define

$$\Psi_b = \sum_{i=1}^{N} (1 - m_i)^2 \,, \tag{36}$$

and the rms error as $\sigma_b = (\Psi_b / N)^{1/2}$.

This approach essentially accepts the magnetometer offset corrections as zero, and pushes the more difficult aspect of the problem back to the manufacturer. The assumption is not as detrimental as one might consider at first, since magnetic signature data is always reported from some, somewhat arbitrary offset, and the offset error only enters into the problem when the magnetic field heading is used to align the sensor data with the earth's magnetic field. The other point is that the offsets as quoted are small.

Thus, by assumption, the magnetometer offsets are zero, and the two magnetometer correction operations simplify to

$$\boldsymbol{B} \Leftarrow \boldsymbol{Q}\,(\boldsymbol{k}\boldsymbol{B})\,, \tag{37}$$

now requiring only the magnetometer scale factors and orthogonality angles to be determined.

In a magnetically quiet area with a uniform and constant magnetic field, it would be possible to adapt the procedure to provide offset corrections, however, an independent value of the background magnetic field would have to be made.

Two methods emerged to parameterize the magnetic field components in terms of some multiple of the applied field and a constant. The first approach was to use least squares minimization to fit the magnetic field components to the applied field and a constant, the second approach was to use the Discrete Fourier Transform (DFT) to determine the harmonic content of the magnetic field components and the applied field, and then take the ratio of the amplitude of the first harmonic of the field component, to the amplitude of the first harmonic of the applied field.

In terms of the final results determined for the multiplier vector $\boldsymbol{m}$ and offset vector $\boldsymbol{b}$, both methods achieved nearly identical results. Some interesting observations concerning the residual errors determined by each method were made. Firstly, since the raw magnetic field components have variations in the tens of thousands of nT while under test, small anomalies in the data can be hidden. The residual error, however,

can be used as a means to determine if an anomaly occurred during the recording process, since the signal portion has been subtracted out. Thus, immediately after each of the recordings, the field components were fitted and the residuals inspected to ensure they were anomaly free, and in the event an anomaly did occur, the measurement was repeated.

As for the residuals themselves, when using the DFT approach the residual was determined by subtracting the fundamental and some number of harmonics from the original signal. As the sine waves were generated with a Tektronix Arbitrary Function Generator AFG3022B, with a signal resolution of 14 bits and oscillator stability of ± 1 ppm, the output frequency was highly stable. Since the function generator and data acquisition system both had high accuracy oscillators, it was possible to record an exact number of oscillations and achieve no spectral leakage. The one downside of the AFG3022B is that the output is digitally generated with a resolution of 14 bits and therefore the sinusoidal output contains signal at the second harmonic, and higher order even harmonics.

For those few cases where drift between the sampling clock and the function generator caused spectral leakage, the residual signal would contain some small sinusoidal content, and for those cases the second method could be used to fit the data using least squares minimization. The DFT approach was found to be significantly faster while the fitted approach often achieved a smaller residual. Theoretically, the fitted approach should always achieve a smaller residual. However, there are slight differences in the frequency response of the differential current monitor and the magnetometer channels which are not accounted for, and as a result the residual typically has greater second harmonic content compared to the DFT approach where the second harmonic content is just subtracted individually for each channel according to the spectral content. Drift was more likely to be observed when the instruments were warming up. It is important to reemphasize that the final results determined for the multiplier vector $\boldsymbol{m}$ and offset vector $\boldsymbol{b}$, were nearly identical using the two methods, provided the measurement was anomaly free and the oscillators operated within specification.

In Fig. 11 is shown an example of the calibration results for a MAG-03 magnetometer. The scale factors and orthogonality angles determined for the example were

$$\begin{bmatrix} k_x & k_y & k_z \end{bmatrix} = \begin{bmatrix} 0.99974 & 0.99868 & 0.99988 \end{bmatrix}, \tag{38}$$

and

$$\begin{bmatrix} \alpha_m & \beta_m & \gamma_m \end{bmatrix} = \begin{bmatrix} 90.349^\circ & 90.089^\circ & 89.972^\circ \end{bmatrix}, \tag{39}$$

respectively, and the rms error decreased by a factor of 51 from 0.21 % to 0.0041 %. As can be seen the scale factors are almost exactly unity indicating excellent agreement with the manufacturer's specifications. The orthogonality angles are defined somewhat differently than specifications so can not be compared directly. The specifications quote an orthogonality error of less than 0.5°. The magnetometer calibration procedure has made the magnetometer error due to scaling and orthogonality misalignment, vanishingly small.

3.4.3 Alignment procedure

Since the solenoid was constructed with its axis of revolution horizontal, the applied field is perpendicular to gravity and therefore the dot product of the applied field and gravity vectors must equal zero regardless of the magnetic node's orientation in the solenoid. Had the solenoid been constructed vertically the dot product would be unity, assuming the relative magnetic field and relative gravity vectors are used. As a result the cost function for the alignment takes the form

$$\Psi_c = \sum_{i=1}^{N} \left(\boldsymbol{A}_i \cdot \boldsymbol{m}_i \right)^2, \tag{40}$$

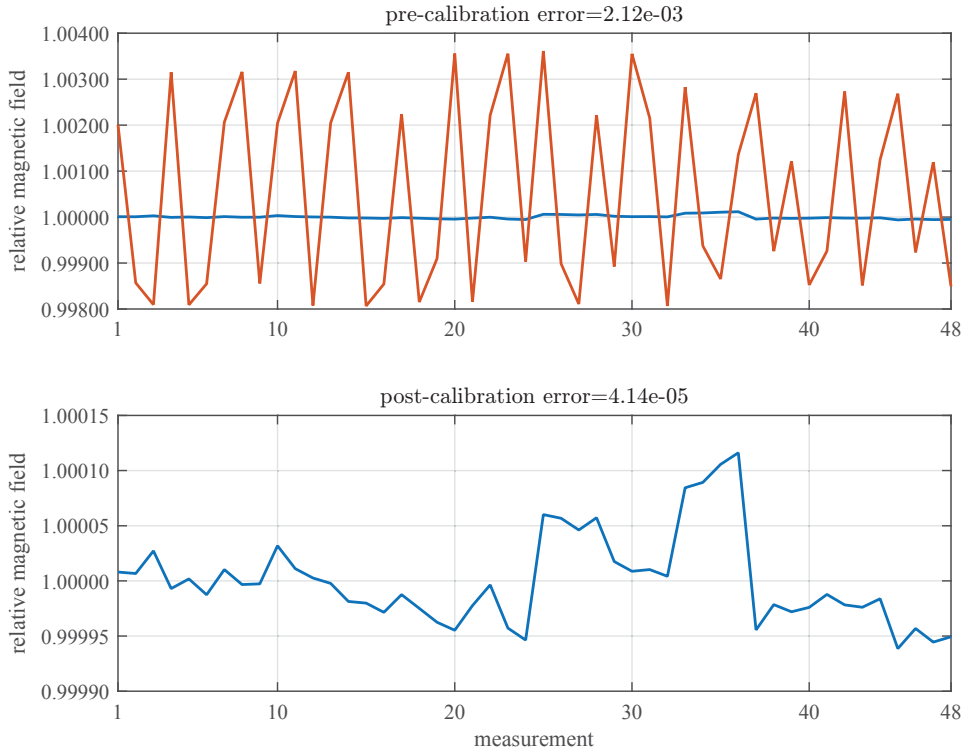

Figure 11: *Magnetometer calibration example: top traces are the relative magnetic field magnitudes before (red) and after (blue) calibration, while the bottom trace shows only the after calibration result.*

where $\boldsymbol{A}_i$ and $\boldsymbol{m}_i$ are the after calibration values of the relative acceleration and relative magnetic field vectors, and the rms error is $\sigma_c = (\Psi_c / N)^{1/2}$.

In Fig. 12 we see the alignment results for the same magnetic node used in the acceleration and magnetometer calibration examples. The graphs show the values of the dot product of the relative acceleration and magnetic field vectors for each measurement. The alignment angles determined for this example were

$$\begin{bmatrix} \psi_x & \phi_y & \theta_z \end{bmatrix} = \begin{bmatrix} -0.305^\circ & 0.906^\circ & 0.915^\circ \end{bmatrix}, \tag{41}$$

and reduced the rms error by a factor of 14 from 1.34 % to 0.095 %. Keep in mind that the initial fitting error of 1.34 % is based on the calibrated values of the magnetometer and accelerometer and would be much greater if the alignment was undertaken prior to the calibrations.

An important consideration of this alignment procedure is that more than a single magnetometer can be mounted to the sensors under test, thus allowing magnetic *gradiometer* sensors to be calibrated. For example, for a full nine axis gradiometer, four three-axis magnetometers can be mounted orthogonally, at some spacing, and each magnetometer can be first aligned to the accelerometer before computing the magnetic field differences. This approach would be superior to that used in [1] because the alignment angles between two magnetometers, using only magnetic field excitation, is not unique and can be achieved by a continuum of solutions.

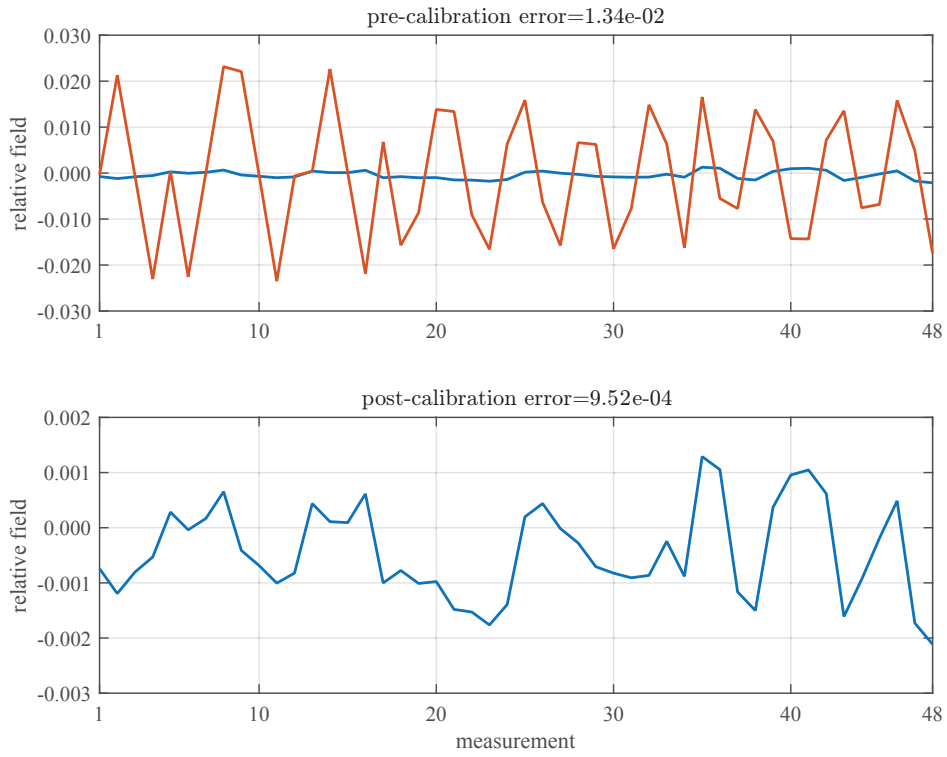

Figure 12: *Alignment calibration example: top traces are the relative acceleration and magnetic field dot products before (red) and after (blue) calibration, while the bottom trace shows only the after calibration result.*

3.5 Analysis of fitting errors

If we combine all the alignment rotations into a single matrix defined as $\boldsymbol{R}_A = \boldsymbol{R}_z\boldsymbol{R}_y\boldsymbol{R}_x$, and the magnetometer calibrations into a single matrix defined as $\boldsymbol{R}_B = \boldsymbol{Q}\boldsymbol{k}$, and, also introduce $\boldsymbol{R}_L$ as a rotation matrix which brings the magnetic field vector to horizontal and vertical, then the combined operations to calibrate and align the magnetic field vector can be represented as

$$\boldsymbol{B} \Leftarrow \boldsymbol{R}_L\boldsymbol{R}_A\boldsymbol{R}_B\boldsymbol{B}. \tag{42}$$

A first order analysis of variance of Eqn. (42) yields the following approximation for the total rms error σ_T of the corrected magnetic field vector

$$\left(1+\sigma_T^2\right) = \left(1+\sigma_a^2\right)\left(1+\sigma_b^2\right)\left(1+\sigma_c^2\right). \tag{43}$$

where σ_a, σ_b, and σ_c correspond to the rms errors for the accelerometer calibration, the magnetometer calibration, and the alignment calibration, introduced previously.

The accelerometer, magnetometer, alignment, and estimated total errors for the example data presented earlier are summarized in Table 1. The calibration and alignment procedure detailed here has clearly improved the measurement accuracy and alignment of the accelerometer and magnetometer. Prior to calibration the total error is estimated at 11.1 %, and is dominated by the accelerometer error. After undergoing the accelerometer and magnetometer calibrations and the alignment procedure, the total error reduces to just 0.12 %, and is primarily due to the remaining accelerometer and alignment errors.

Table 1: *Percentage rms error before and after calibration for the accelerometer (σ_a), the magnetometer (σ_b), the alignment process (σ_c) and the total error (σ_T).*

rms error (%)	σ_a	σ_b	σ_c	σ_T
before	11.0	0.21	1.34	11.1
after	0.072	0.0041	0.095	0.12

4. Conclusions

A robust procedure for the calibration and alignment of collocated three-axis magnetometers and three-axis accelerometers has been presented. The procedure includes the design of a solenoid which creates a highly uniform magnetic field by adjusting first the number of turns and then the position of the outer three loops. Calibration models for both the accelerometer and magnetometer were then introduced, as well as a yaw, pitch and roll alignment model for the two sensors. Preliminary testing revealed better convergence when the test orientations were selected to maximize the measured field components, analogous to spreading the points on a line, and led to the use of 48 measurement positions, which could be achieved through two 45° rotations on any two axes, creating relative field levels of $\sqrt{2}/2$ on one axis and $1/2$ on the other two axes. The fitting procedures for the accelerometer and magnetometer are based on the magnitude of the acceleration and magnetic fields and therefore the exact sensor positions and orientations are not critical and do not need to be known, eliminating the need for an accurately aligned gimbal system. For the magnetometer, the component field values were parameterized in terms of alternating and constant components, and the residuals inspected for anomalies. By equating the magnitude of the magnetic field in solenoid coordinates and magnetometer coordinates, it was discovered the magnetometer scale and orthogonality angles could be determined by fitting the magnitude of the alternating components to unity. In high gradient fields, the procedure does not provide offset corrections for the magnetometer, however, the selected magnetometer has excellent offset specifications allowing this value to be reasonably ignored. Calibration results for both the accelerometer and magnetometer were in excellent agreement with manufacturer's specifications. Since the solenoid was constructed horizontally the applied magnetic field is perpendicular to gravity, allowing the determination of the alignment angles since the dot product of the applied magnetic field and gravity is zero. Since multiple magnetometers can be aligned to a single accelerometer the procedure can also be used to calibrate magnetic gradiometers. Analysis of the fitting error revealed that the total error reduced from 11.1 % to 0.12 % after all stages of the calibration procedure were performed.

Acknowledgements

The realization of the solenoid was made possible by the attention to detail, and perseverance, of Richard Religa. The design and development of the differential current monitor was provided by George Schattschneider, analog electrical engineer extraordinaire, who literally dreamt the circuit up. To both, your support and comradery, as always, is greatly appreciated. And a special thank you to Nicos Pelavas for his critical discussions and thorough review.

References

[1] Robert E. Bracken, David V. Smith, and Philip J. Brown. Calibrating a tensor magnetic gradiometer using spin data. Scientific Investigations Report 2005-5045, U.S. Geological Survey, 2005.

[2] John David Jackson. *Classical Electrodynamics*. John Wiley and Sons, 3^{rd} edition, 1975.

[3] N. Nouri and B. Plaster. Comparison of magnetic field uniformities for discretized and finite-sized standard $\cos\theta$, solenoidal, and spherical coils. *Nucl.Instrum.Methods Phys.Res.*, A723:30, 2013.

[4] Justin Peter Dinale. Magnetic test facility - sensor and coil calibrations, 2013. in conjunction with Defence Science and Technology Organisation, Australian Department of Defence.

[5] S. Magdaleno-Adame, J.C. Olivares-Galvan, E. Campero-Littlewood, and R. Escarela-Perez. Coil systems to generate uniform magnetic field volumes. In *Proceedings of the COMSOL Conference*, Boston, 2010.

[6] Nilangshu K. Das, Parthasarathi Barat, Sounak Dey, and Tammana Jayakumar. Design of miniature coil to generate uniform magnetic field. *Progress In Electromagnetics Research M (PIER M)*, 34:99–105, 2014.

[7] Matlab ©. *Optimization Toolbox User's Guide*. The MathWorks, Inc., Natick, Massachusetts, USA, 2015.

[8] Geometrics. *G-824A Cesium Magnetometer*. Geometrics, Inc., SanJose, CA, USA, 2014.

[9] TT Electronics. *Nichrome Resistor Networks on Ceramic Substrates Model 694, 698, 699 Series data sheet*. BI Technologies, Fullerton, CA, USA, 2014.

[10] Bartington Instruments. *Mag-03 Three Axis Magnetic Field Sensors*. Bartington Instruments Limited, Oxford, England, 2014.

[11] Analog Devices. *ADXL327 Small, Low Power, 3-Axis ±2 g Accelerometer*. Analog Devices, Norwood, MA, USA, 2014.

[12] Duane Watson. Transportable underwater range for naval signatures, user guide - contractor report. Contractor Report 2387, Omnitech Electronics Inc., 2014.

[13] Freescale Semiconductor. *High Precision Calibration of a Three-Axis Accelerometer*. Freescale Semiconductor Inc, Autin, Texas, USA, 2014.

[14] Exelis ©. *IDL - Interactive Data Language*. Exelis Visual Information Solutions, Boulder, Colorado, USA, 2015.

[15] National Instruments ©. *LabVIEW development system*. National Instruments Corporation, Austin, TX, USA, 2015.

[16] Robert A. Schill Jr. General relation for the vector magnetic field of a circular current loop: a closer look. *IEEE Transactions on Magnetics*, 39:961–967, March 2003.

[17] Julius Adams Stratton. *Electromagnetic Theory*. McGraw-Hill Publishing Company, 1941.

A. Magnetic field of an arbitrarily located current segment

The magnetic field produced by an arbitrarily located straight line segment can be determined using the Biot-Savart Law, and by superimposing the results from multiple segments, provides a useful building block to determine the magnetic field of complex configurations. According to the Biot-Savart Law a differential current element $d\boldsymbol{l}$ will produce a magnetic field $d\boldsymbol{B}$ given as

$$d\boldsymbol{B} = \frac{\mu_0 I}{4\pi}\left(\frac{d\boldsymbol{l}\times\boldsymbol{R}}{R^3}\right), \tag{44}$$

where $\boldsymbol{R}$ is the vector from the differential current element to the observation point, and $R = |\boldsymbol{R}|$.

For the current segment shown in Fig. 13 the path of the current is defined from $P_a\,(x_a, y_a, z_a)$ to $P_b\,(x_b, y_b, z_b)$, and the magnetic field is to be determined at the observation point $P\,(x, y, z)$. If the solution from multiple current segments are superimposed, with each additional start point connected to the previous end point, the resulting current path becomes realizable when the path closes on itself.

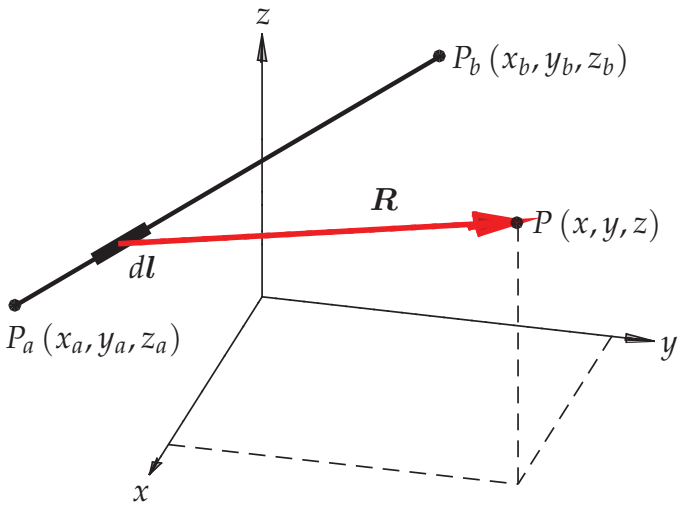

Figure 13: *Magnetic field of a current segment from $P_a\,(x_a, y_a, z_a)$ to $P_b\,(x_b, y_b, z_b)$.*

To facilitate the derivation, the position vector $\boldsymbol{R}_1$ is introduced to describe the location of the differential current element, and the current path is parameterized in terms of an integration variable t, such that

$$\boldsymbol{R}_1\,(t) = \boldsymbol{a}_x\,[x_a + (x_b - x_a)\,t] + \boldsymbol{a}_y\,[y_a + (y_b - y_a)\,t] + \boldsymbol{a}_z\,[z_a + (z_b - z_a)\,t]\,, \tag{45}$$

where $\boldsymbol{a}_x$, $\boldsymbol{a}_y$ and $\boldsymbol{a}_z$ are unit vectors in the x, y and z directions respectively. Noting that $\boldsymbol{R}_1\,(0) = \boldsymbol{a}_x\,x_a + \boldsymbol{a}_y\,y_a + \boldsymbol{a}_z\,z_a$ and $\boldsymbol{R}_1\,(1) = \boldsymbol{a}_x\,x_b + \boldsymbol{a}_y\,y_b + \boldsymbol{a}_z\,z_b$, the required current segment is described on $0 \le t \le 1$. Applying the chain rule, the differential current element is determined as

$$d\boldsymbol{l} = \frac{d\boldsymbol{R}_1}{dt}\,dt = \left[\boldsymbol{a}_x\,(x_b - x_a) + \boldsymbol{a}_y\,(y_b - y_a) + \boldsymbol{a}_z\,(z_b - z_a)\right]dt. \tag{46}$$

The position vector, $\boldsymbol{R}$, is given as

$$\boldsymbol{R} = \boldsymbol{a}_x\,[(x - x_a) - (x_b - x_a)\,t] + \boldsymbol{a}_y\,[(y - y_a) - (y_b - y_a)\,t] + \boldsymbol{a}_z\,[(z - z_a) - (z_b - z_a)\,t] \tag{47}$$

and the explicit notation that $\boldsymbol{R}$ is function of t has been dropped. Introducing

$$\begin{array}{lll} \delta_x = x - x_a, & \delta_y = y - y_a, & \delta_z = z - z_a \\ \Delta_x = x_b - x_a, & \Delta_y = y_b - y_a, & \Delta_z = z_b - z_a \\ \lambda_x = x - x_b, & \lambda_y = y - y_b, & \lambda_z = z - z_b, \end{array}$$

$\boldsymbol{R}$ and $d\boldsymbol{l}$ simplify to

$$\boldsymbol{R} = \boldsymbol{a}_x \ (\delta_x - \Delta_x \, t) + \boldsymbol{a}_y \ \left(\delta_y - \Delta_y \, t\right) + \boldsymbol{a}_z \ (\delta_z - \Delta_z \, t) \tag{48}$$

and

$$d\boldsymbol{l} = \left[\boldsymbol{a}_x \, \Delta_x + \boldsymbol{a}_y \, \Delta_y + \boldsymbol{a}_z \, \Delta_z\right] dt. \tag{49}$$

Substituting these results into Eqn. (44) and integrating, the magnetic field of the current segment is

$$\boldsymbol{B} = \frac{\mu_0 I}{4\pi} \left[\boldsymbol{a}_x \ \left(\Delta_y \delta_z - \Delta_z \delta_y\right) + \boldsymbol{a}_y \ \left(\Delta_z \delta_x - \Delta_x \delta_z\right) + \boldsymbol{a}_z \ \left(\Delta_x \delta_y - \Delta_y \delta_x\right)\right] \int_0^1 \frac{1}{R^3} \, dt, \tag{50}$$

where it is noted that the cross product $d\boldsymbol{l} \times \boldsymbol{R}$ is independent of t. Evaluating the integral, the final form of the solution for the magnetic field of an arbitrarily located straight line current segment is

$$\begin{aligned} \boldsymbol{B} = & \frac{\mu_0 I}{4\pi} \left[\frac{\Delta_x \delta_x + \Delta_y \delta_y + \Delta_z \delta_z}{\delta_x^2 + \delta_y^2 + \delta_z^2} - \frac{\Delta_x \lambda_x + \Delta_y \lambda_y + \Delta_z \lambda_z}{\lambda_x^2 + \lambda_y^2 + \lambda_z^2}\right] \\ & \left[\frac{\boldsymbol{a}_x \ \left(\Delta_y \delta_z - \Delta_z \delta_y\right) + \boldsymbol{a}_y \ \left(\Delta_z \delta_x - \Delta_x \delta_z\right) + \boldsymbol{a}_z \ \left(\Delta_x \delta_y - \Delta_y \delta_x\right)}{\left(\Delta_y \delta_z - \Delta_z \delta_y\right)^2 + \left(\Delta_z \delta_x - \Delta_x \delta_z\right)^2 + \left(\Delta_x \delta_y - \Delta_y \delta_x\right)^2}\right]. \end{aligned} \tag{51}$$

B. Magnetic field of a current loop

The magnetic field produced by a circular current loop can be determined by taking the curl of the vector potential as shown in [16, 17], however, the solution can also be obtained using the Biot-Savart Law. For the circular current loop shown in Fig. 14 the loop has a radius of a and the magnetic field is to be determined at the observation point $P\,(x, y, z)$.

The differential current element can then be expressed as

$$d\boldsymbol{l} = \left(-\boldsymbol{a}_x \ \sin\phi + \boldsymbol{a}_y \ \cos\phi\right) a \, d\phi, \tag{52}$$

where ϕ is the integration path variable. The vector $\boldsymbol{R}$ from the differential current element to the observation point then becomes

$$\boldsymbol{R} = \boldsymbol{a}_x \ (x - a\cos\phi) + \boldsymbol{a}_y \ (y - a\sin\phi) + \boldsymbol{a}_z \, z. \tag{53}$$

Introducing the cylindrical coordinate variables r and θ where $x = r\cos\theta$ and $y = r\sin\theta$, the magnitude squared of $\boldsymbol{R}$ simplifies to

$$R^2 = a^2 + r^2 + z^2 - 2ar\cos\left(\phi - \theta\right) \tag{54}$$

and

$$d\boldsymbol{l} \times \boldsymbol{R} = \left(\boldsymbol{a}_x \, z\cos\phi + \boldsymbol{a}_y \, z\sin\phi + \boldsymbol{a}_z \ \left[a - r\cos\left(\phi - \theta\right)\right]\right) a \, d\phi. \tag{55}$$

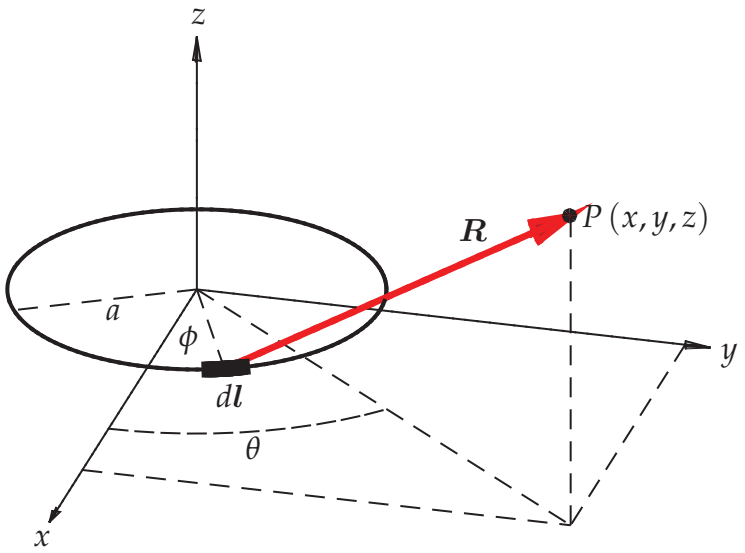

Figure 14: *Magnetic field of a circular current loop of radius a.*

Substituting these results into the Biot-Savart Law, integrating over the current path, then expanding the trigonometric terms, changing the integration variable $\phi \rightarrow \phi + \theta$, and recognizing even and odd symmetries, the magnetic field simplifies to

$$\boldsymbol{B} = \frac{\mu_0 I}{2\pi} \int_0^{\pi} \frac{\boldsymbol{a}_x \, z \cos\theta \cos\phi + \boldsymbol{a}_y \, z \sin\theta \sin\phi + \boldsymbol{a}_z \, (a - r\cos\phi)}{\left(a^2 + r^2 + z^2 - 2ar\cos\phi\right)^{3/2}} a \, d\phi. \tag{56}$$

The required integrals can be expressed in terms of the complete elliptical integrals yielding

$$\begin{aligned} \boldsymbol{B} = \frac{\mu_0 I}{2\pi \left[(r+a)^2 + z^2\right]^{1/2}} \Bigg[& \left(\boldsymbol{a}_x \frac{z}{r}\cos\theta + \boldsymbol{a}_y \frac{z}{r}\sin\theta\right) \left(E(k) \frac{r^2 + a^2 + z^2}{(r-a)^2 + z^2} - K(k)\right) \\ & + \boldsymbol{a}_z \left(E(k) \frac{a^2 - r^2 - z^2}{(r-a)^2 + z^2} - K(k)\right) \Bigg] \end{aligned} \tag{57}$$

where $E(k)$ and $K(k)$ are the complete elliptical integrals of the first and second kind respectively, and

$$k^2 = \frac{4ar}{(r+a)^2 + z^2}. \tag{58}$$